The Astrophysical Journal Letters, 826:L8 (8pp), 2016 July 20 doi:10.3847/2041-8205/826/1/L8
© 2016. The American Astronomical Society. All rights reserved.

CALIBRATION OF EVOLUTIONARY DIAGNOSTICS IN HIGH-MASS STAR FORMATION

S. Molinari[1], M. Merello[1], D. Elia[1], R. Cesaroni[2], L. Testi[2,3,4], and T. Robitaille[5]
[1] Istituto Nazionale di Astrofisica—IAPS, Via Fosso del Cavaliere 100, I-00133 Roma, Italy; molinari@iaps.inaf.it
[2] Istituto Nazionale di Astrofisica—Osservatorio di Arcetri, Largo E. Fermi 5, I-50125 Firenze, Italy
[3] European Southern Observatory, Garching, Germany
[4] Excellence Cluster universe, Boltzmannstr. 2, D-85748 Garching, Germany
[5] Max Planck Institut für Astronomie, Heidelberg, Germany
Received 2016 February 17; revised 2016 April 20; accepted 2016 April 20; published 2016 July 15

ABSTRACT

The evolutionary classification of massive clumps that are candidate progenitors of high-mass young stars and clusters relies on a variety of independent diagnostics based on observables from the near-infrared to the radio. A promising evolutionary indicator for massive and dense cluster-progenitor clumps is the *L/M* ratio between the bolometric luminosity and the mass of the clumps. With the aim of providing a quantitative calibration for this indicator, we used SEPIA/APEX to obtain $CH_3C_2H(J = 12–11)$ observations, which is an excellent thermometer molecule probing densities $\geqslant 10^5$ cm^{-3}, toward 51 dense clumps with $M \geqslant 1000 M_\odot$ and uniformly spanning $-2 \lesssim \mathrm{Log}(L/M)\ [L_\odot/M_\odot] \lesssim 2.3$. We identify three distinct ranges of *L/M* that can be associated to three distinct phases of star formation in massive clumps. For $L/M \leqslant 1$ no clump is detected in CH_3C_2H, suggesting an inner envelope temperature below ∼30K. For $1 \lesssim L/M \lesssim 10$ we detect 58% of the clumps with a temperature between ∼30 and ∼35 K independently from the exact value of *L/M*; such clumps are building up luminosity due to the formation of stars, but no star is yet able to significantly heat the inner clump regions. For $L/M \gtrsim 10$ we detect all the clumps with a gas temperature rising with Log(*L/M*), marking the appearance of a qualitatively different heating source within the clumps; such values are found toward clumps with UCH II counterparts, suggesting that the quantitative difference in *T* versus *L/M* behavior above $L/M \sim 10$ is due to the first appearance of ZAMS stars in the clumps.

Key words: ISM: clouds – ISM: molecules – stars: formation – stars: protostars

1. INTRODUCTION

Molecular clumps, massive ($M \geqslant 10^3\ M_\odot$), and cold ($T \leqslant 30$ K) condensations of dense gas and dust ($\Sigma \geqslant 0.1$g cm^{-2}) with sizes between 0.1 and few parsecs are the primary sites for the formation of stellar clusters. Either by the accretion of turbulent cores fragmenting into the clump (McKee & Tan 2003) or by a more dynamical process of competitive accretion where initial seeds migrate within the clump hunting for material to accrete (Bonnell et al. 2001), clump-hosted protoclusters are the sites where intermediate and high-mass stars form (e.g., Testi et al. 1999; de Wit et al. 2004; Faustini et al. 2009). There is evidence that clumps hosting massive cores in the very early stages of formation are already associated with populations of lower-mass YSOs visible in the near-IR, hence relatively more evolved (e.g., Faustini et al. 2009). Although the early products in clump-hosted protoclusters appear to be relatively low-mass YSOs, the appearance of intermediate and high-mass forming protostars is the event that drives the radiative energy budget in these systems. Molinari et al. (2008) showed that the massive forming objects accreting with a rate proportional to their mass (McKee & Tan 2003) show a dramatic increase in radiated bolometric luminosity as a function of time while their core envelope mass decreases only slightly; this can be followed very conveniently in a $L_{\rm bol}$–$M_{\rm env}$ diagram (see Figure 3), where simple-model evolutionary tracks mark the path of star-forming clumps along three basic phases. Initially, clumps are "pre-stellar" or undergoing very low rates of star formation (red dots), with an SED resembling very well a modified blackbody with no detectable continuum at $\lambda \leqslant 100\ \mu$m. In a second phase that we call "protostellar," the clump starts to exhibit far-infrared continuum radiation well in excess of a single-temperature modified blackbody; this is interpreted as the indication that ongoing star formation becomes able to significantly heat the clump's interior (the blue dots). As accretion proceeds, the clumps increase their luminosity more and more (following the ascending portion of the model evolutionary tracks in Figure 3) until they reach the luminosity typical for UltraCompact (UC)H II regions (see Figure 9 of Molinari et al. 2008). Subsequent evolution is modeled as envelope dispersal by stellar winds and outflows. Independent evolutionary indications from the association with methanol masers or radio continuum (Sanchez-Monge et al. 2013) or with the properties of ammonia dense gas (Giannetti et al. 2013) are consistent with the predictions in Molinari et al. (2008).

With the Hi-GAL project (Molinari et al. 2010, 2016) we detected and characterized several tens of thousands of dense clumps (D. Elia et al. 2016, in preparation), enabling statistical studies mapping star formation history and rates throughout the Milky Way (Veneziani et al. 2013, 2016). It is then important that star formation rate (SFR) probes as well as evolutionary tools like the $L_{\rm bol}$–$M_{\rm env}$ diagrams are better and better characterized and calibrated against indicators that can independently probe the temperatures of the gas in the innermost regions of massive clumps, where the most massive YSOs are forming. Among the best tracers in this respect is CH_3C_2H (methyl-acetylene), which is optically thin in most typical conditions in massive clumps and whose *K*-ladder rotational transitions are collisionally excited at densities in excess of 10^5cm^{-3} (e.g., Bergin et al. 1994; Brand et al. 2001; Fontani et al. 2002, 2004; Thompson & Macdonald 2003).

2. OBSERVATIONS

2.1. Target Selection

Dense and massive clumps in the active phase of star formation were selected from the Hi-GAL survey (Molinari et al. 2010, 2016; D. Elia et al. 2016, in preparation). A first list is established by selecting Hi-GAL sources with counterparts in at least four adjacent Herschel bands including the 70 μm band and with an available determination of a heliocentric distance (Russeil et al. 2011). The submillimeter portion of the continuum SED in these clumps is fitted with a modified graybody whose temperature represents the bulk of the cold dust in the clumps and that provides negligible contribution for $\lambda \leqslant 100\,\mu$m; the presence of a 70 μm counterpart is therefore in excess of this cold clump emission and is generally assumed as an indication of ongoing star formation inside the clumps.

We restricted objects in the longitude range $-10^\circ \leqslant l \leqslant -60^\circ$ and with a 350 μm flux $\geqslant$10 Jy to be in the best detection conditions irrespective of the target distance. We then selected the clumps with $M \geqslant 1000\ M_\odot$ that can generate intermediate and high-mass protostars and that have a distance $\lesssim$10 kpc. The resulting sample of objects, conveniently distributed on the far tip of the Galactic Bar, the Norma, Scutum, and Sagittarius arms, was finally skimmed down to 51 sources by sampling the distribution of the *L/M* values to uniformly cover (in log values) the range of *L/M* from the initial protostellar phase (*L/M* $\sim$ 0.01, albeit with a 70 μm counterpart) to the UCH II phase with *L/M* $\gtrsim$ 100 (hereinafter in units of $L_\odot/M_\odot$). Target positions and properties from D. Elia et al. (2016, in preparation) are reported in Table 1; sources distribution in *L/M* is uniform as a function of distance so that no distance bias is present in the target sample.

2.2. Data Analysis

Observations of the CH_3C_2H(J = 12–11) lines ladder (K = 0, 3) at ν = 205.08073–205.01811 GHz toward the target clumps were carried out using the new SEPIA receiver equipped with a Band 5 ALMA pre-production cartridge (Billade et al. 2012) at the ESO Atacama Pathfinder EXperiment telescope, with a main beam HPBW $\sim$30″. Data were acquired in ON–OFF mode toward the 70 μm peak position of each clump; thanks to values of 0.4–0.45 mm of precipitable water vapor, we could reach typical rms values in 0.112 km s^{-1} channels between 50 and 60 mK (in $T_{\rm MB}$, see below) in about 12 minutes integration time on average. More time could be spent on a few sources, pushing the rms down to values between 20 and 40 mK, hence improving the signal-to-noise ratio of the detected lines. The CLASS software package was used to accumulate spectra and subtract a first-order baseline. Antenna temperatures were converted into main-beam temperatures using an efficiency of $\eta_{\rm mb}$ = 0.8 (C. de Breuck 2016, private communication). The spectra obtained for the detected sources are reported in Figure 1, with the location of the four K-ladder components marked by vertical ticks. Simultaneous four-component Gaussian fitting was performed in CLASS, fixing the frequency separation among the different K components to the laboratory values and forcing their line widths to be all equal. In some cases sources with marginal detections of the higher K components did not yield convergence in the fitting and they were neglected in subsequent analysis (see Table 1).

Integrated line fluxes obtained from the Gaussian fitting are reported in Table 1 and were used to compute Boltzmann plots (i.e., the rotational diagram) relating the column density of the emitters normalized by the level degeneracy and the energy of the levels. Using standard procedures (e.g., Fontani et al. 2002), assuming LTE and optically thin conditions that are appropriate for this line and class of sources (e.g., Bergin et al. 1994) the temperature and total column density of CH_3C_2H can be derived from a linear fit to the rotational diagram (Goldsmith & Langer 1999). Because our observations are single-pointed toward the 70 μm peak of the sources, we could only derive beam-averaged column densities and we chose to focus on the analysis of the CH_3C_2H rotational temperatures (see Table 1).

3. RESULTS

3.1. CH_3C_2H Detection Statistics

The sources listed in Table 1 are ordered according to their *L/M* value computed from the Herschel fluxes, augmented with ancillary data at mid-IR wavelengths (D. Elia et al. 2016, in preparation), and it can be immediately seen that the detection rate in CH_3C_2H(J = 12–11) is strongly dependent on the *L/M* values. We can distinguish three ranges of *L/M*: the rate is 0 (none out of 23 sources) for the sources with *L/M* < 1, 58% (seven out of 12) for sources with 1 < *L/M* < 10 and 90% (16 out of 18 sources) for sources with *L/M* > 10. In Table 1, in sources # 32, 35, and 38, at least the K = 0 line is detected, but the four-component Gaussian fit to the four lines did not converge and so no further analysis could be carried out for these sources.

This finding is preliminary confirmation of the working hypothesis that higher values of *L/M* should be related with a more advanced evolutionary stage. As CH_3C_2H is a temperature probe for gas with densities in excess of 10^5 cm^{-3} (Bergin et al. 1994), its values are influenced more by the inner clump regions and relatively less by the outer envelope. Looking at Figure 3, the range of *L/M* $\lesssim$ 1 is characteristic of "pre-stellar" clumps (in which, contrary to the sources of the present study, 70 μm emission is not detected); the internal input energy producing the detectable 70 μm flux would not seem sufficient to drive up considerably the bolometric luminosity as well as the internal clump temperature, resulting in non-detections in CH_3C_2H(J = 12–11) for any of the sources with *L/M* < 1. This suggests that in these clumps intermediate or high-mass star formation has not yet started.

Above the *L/M* = 1 threshold, corresponding to the upper envelope of the "pre-stellar" clumps distribution in Figure 3, the CH_3C_2H(J = 12–11) detection rate increases sharply, implying that the internal energy produced by star formation is rising to levels sufficient to heat up the inner envelope gas to at least $\sim$30K. The dust temperature estimated using Herschel data D. Elia et al. (2016, in preparation) in these clumps is on average 60% lower, confirming that the CH_3C_2H(J = 12–11) line detected is excited in the inner regions of the clumps compared to the more external regions where the $\lambda \geqslant 100\,\mu$m continuum is generated.

Miettinen et al. (2006) report a CH_3C_2H abundance that is proportional to temperature in a sample of dense clumps, a result that is interpreted as evidence of desorption from grain ice mantles. The sharp rise in CH_3C_2H(J = 12–11) detection

Table 1
Sources Sample and Results; Sources Are Ordered in Increasing *L/M*

#	R.A.	Decl.	Dist	Mass	*L/M*	rms	CH_3C_2H (12–11) Integrated Intensity (K · km s^{-1})[a]				Δv	T [CH_3C_2H]	T_{dust}
	(^{h} $'$ $''$)	($^\circ$ $'$ $''$)	(kpc)	(10^4 $M_\odot$)	($L_\odot/M_\odot$)	(mK)[a]	($K = 0$)	($K = 1$)	($K = 2$)	($K = 3$)	(km s^{-1})	(K)	(K)
1	15 43 51.9	−53 58 11.3	2.77	1.58	0.01	49	…	…	…	…	…	…	7.8
2	14 10 11.8	−61 42 59.3	7.76	2.87	0.01	53	…	…	…	…	…	…	7.7
3	15 32 50.5	−55 58 08.2	10.3	21.2	0.01	50	…	…	…	…	…	…	7.6
4	16 02 15.1	−53 21 59.2	9.8	8.1	0.01	48	…	…	…	…	…	…	7.0
5	16 27 56.9	−47 19 45.0	5.1	0.62	0.01	53	…	…	…	…	…	…	7.3
6	14 21 44.0	−60 52 09.0	8.2	1.18	0.02	54	…	…	…	…	…	…	7.9
7	16 55 04.8	−43 14 34.8	5.0	1.41	0.02	49	…	…	…	…	…	…	8.7
8	15 46 26.2	−53 55 46.9	10.7	1.78	0.03	52	…	…	…	…	…	…	8.2
9	16 11 16.4	−52 02 57.7	4.2	0.53	0.03	51	…	…	…	…	…	…	8.9
10	15 56 31.6	−52 38 03.0	8.6	1.09	0.04	47	…	…	…	…	…	…	8.2
11	17 02 43.6	−42 20 53.7	10.6	0.89	0.05	51	…	…	…	…	…	…	8.8
12	16 37 58.7	−47 08 56.0	10.7	2.16	0.06	51	…	…	…	…	…	…	9.2
13	16 34 13.7	−47 51 18.7	8.4	1.3	0.08	51	…	…	…	…	…	…	9.6
14	16 23 26.8	−49 29 55.5	9.8	0.86	0.10	51	…	…	…	…	…	…	9.2
15	14 39 26.0	−60 01 54.0	8.8	0.63	0.12	53	…	…	…	…	…	…	9.7
16	15 16 32.5	−58 08 31.3	9.4	0.91	0.15	51	…	…	…	…	…	…	9.9
17	16 35 27.5	−47 49 32.8	7.2	0.58	0.18	50	…	…	…	…	…	…	10.9
18	15 51 00.9	−54 26 50.8	10.4	1.78	0.24	49	…	…	…	…	…	…	11.2
19	17 14 21.7	−39 29 21.8	10.5	0.60	0.30	53	…	…	…	…	…	…	10.9
20	16 12 38.5	−51 37 32.8	9.86	0.52	0.37	53	…	…	…	…	…	…	12.1
21	13 12 22.8	−62 34 59.4	5.9	2.0	0.49	50	…	…	…	…	…	…	12.2
22	15 14 32.2	−58 11 22.2	8.24	0.60	0.59	51	…	…	…	…	…	…	13.6
23	16 10 19.7	−51 49 44.9	9.3	0.60	0.73	46	…	…	…	…	…	…	14.1
24	11 15 12.3	−61 18 52.0	8.12	0.83	1.0	14	0.115 ± 0.015	0.106 ± 0.015	0.053 ± 0.016	0.035 ± 0.016	4.19	36.1 ± 4.4	13.8
25	13 11 17.1	−62 46 38.5	6.94	0.59	1.1	53	0.458 ± 0.041	0.380 ± 0.038	0.134 ± 0.040	0.145 ± 0.038	2.67	34.4 ± 4.5	15.9
26	16 34 56.4	−47 34 37.2	10.8	0.70	1.7	50	0.205 ± 0.048	0.175 ± 0.052	0.083 ± 0.041	0.063 ± 0.041	3.41	34.9 ± 1.6	16.5
27	17 17 32.7	−37 39 31.8	11.2	0.72	2.0	53	…	…	…	…	…	…	14.8
28	15 32 14.4	−55 52 31.6	10.3	0.63	2.4	40	…	…	…	…	…	…	13.7
29	17 11 25.9	−39 09 12.0	5.76	0.58	2.9	53	0.533 ± 0.044	0.522 ± 0.044	0.218 ± 0.041	0.168 ± 0.040	3.1	34.9 ± 5.4	18.9
30	16 41 43.3	−46 18 39.8	9.9	0.67	3.3	49	…	…	…	…	…	…	16.8
31	13 12 48.4	−62 36 15.7	6.76	0.18	4.6	35	…	…	…	…	…	…	15.2
32	16 12 07.1	−51 58 30.9	10.5	1.93	5.6	54	…[b]	…[b]	…	…	…	…	16.1
33	16 12 02.0	−52 00 53.2	10.5	1.55	7.1	54	0.353 ± 0.037	0.356 ± 0.038	0.127 ± 0.034	0.094 ± 0.034	2.21	31.8 ± 6.7	17.4
34	14 03 35.4	−61 18 23.8	6.2	0.17	7.9	36	…	…	…	…	…	…	16.7
35	13 11 48.0	−62 46 39.5	6.9	0.11	8.4	20	…[b]	…[b]	…	…	…	…	20.9
36	14 26 08.3	−60 40 21.4	7.9	0.19	10.3	24	…	…	…	…	…	…	17.9
37	12 03 16.6	−63 11 17.7	11.1	0.59	11.5	22	0.350 ± 0.020	0.136 ± 0.014	0.106 ± 0.014	0.100 ± 0.014	2.88	36.8 ± 3.3	21.6
38	16 12 07.3	−51 30 01.1	9.5	0.57	12.8	45	…[b]	…[b]	…	…	…	…	24.4
39	13 11 14.5	−62 47 25.6	6.94	0.14	19.8	34	0.575 ± 0.030	0.567 ± 0.031	0.248 ± 0.029	0.243 ± 0.029	2.96	40.9 ± 6.1	27.9
40	16 48 05.2	−45 05 07.1	9.3	0.59	21.3	53	0.575 ± 0.038	0.514 ± 0.040	0.241 ± 0.037	0.164 ± 0.037	3.01	34.2 ± 2.9	22.9
41	15 00 55.1	−58 58 50.4	10.4	0.62	22.8	53	1.020 ± 0.045	0.768 ± 0.042	0.440 ± 0.041	0.281 ± 0.048	2.49	34.4 ± 2.1	32.0
42	16 01 01.7	−52 38 51.2	8.27	0.17	23.6	35	0.192 ± 0.025	0.180 ± 0.026	0.068 ± 0.023	0.059 ± 0.023	1.98	33.6 ± 5.0	20.0
43	11 15 10.6	−61 20 33.4	8.12	0.18	25.1	20	0.730 ± 0.022	0.653 ± 0.020	0.355 ± 0.200	0.240 ± 0.019	3.47	37.7 ± 2.7	31.8
44	16 36 43.1	−47 31 22.9	10.9	1.41	28.3	51	4.687 ± 0.049	4.043 ± 0.048	2.500 ± 0.046	1.964 ± 0.048	3.85	43.8 ± 1.6	24.5
45	16 35 33.9	−47 31 10.7	10.9	0.85	28.9	52	1.181 ± 0.038	1.098 ± 0.038	0.311 ± 0.037	0.460 ± 0.037	3.67	38.4 ± 7.9	36.3

Table 1
(Continued)

#	R.A.	Decl.	Dist	Mass	*L/M*	rms	CH_3C_2H (12–11) Integrated Intensity ($K \cdot km\ s^{-1}$)[a]				Δv	T [CH_3C_2H]	T_{dust}
	($^h\ ^\prime\ ^{\prime\prime}$)	($^\circ\ ^\prime\ ^{\prime\prime}$)	(kpc)	($10^4\ M_\odot$)	($L_\odot/M_\odot$)	(mK)[a]	($K = 0$)	($K = 1$)	($K = 2$)	($K = 3$)	($km\ s^{-1}$)	(K)	(K)
46	15 09 52.4	−58 25 33.8	8.24	0.24	36.5	36	1.368 ± 0.035	1.192 ± 0.033	0.790 ± 0.034	0.412 ± 0.034	3.62	40.3 ± 6.5	36.9
47	13 32 35.5	−62 45 29.5	7.2	0.17	38.1	35	0.275 ± 0.023	0.221 ± 0.022	0.102 ± 0.022	0.125 ± 0.022	1.73	43.9 ± 5.7	36.9
48	16 21 32.4	−50 26 47.5	3.55	0.24	52.1	35	2.870 ± 0.034	2.483 ± 0.033	1.405 ± 0.031	1.103 ± 0.033	3.93	40.9 ± 1.2	25.2
49	12 09 58.0	−62 49 35.8	11.35	0.86	72.0	15	0.176 ± 0.014	0.136 ± 0.014	0.106 ± 0.012	0.100 ± 0.014	3.52	56.5 ± 6.1	21.0
50	16 20 11.4	−50 53 12.2	3.85	0.46	77.0	38	7.698 ± 0.008	7.043 ± 0.041	4.163 ± 0.042	3.878 ± 0.001	4.98	49.2 ± 0.3	24.0
51	15 54 06.4	−53 11 37.8	8.44	0.55	185	52	1.308 ± 0.049	1.321 ± 0.049	0.682 ± 0.049	0.886 ± 0.050	4.5	58.9 ± 9.4	32.9

Notes.
[a] Main-beam temperatures, assuming $\eta_{mb} = 0.8$; the reported rms is for 0.112 $km\ s^{-1}$ channels.
[b] $K = 0$, 1 lines are detected, but no convergence was found in the simultaneous $K = 0$, 1, 2, 3 line fitting.

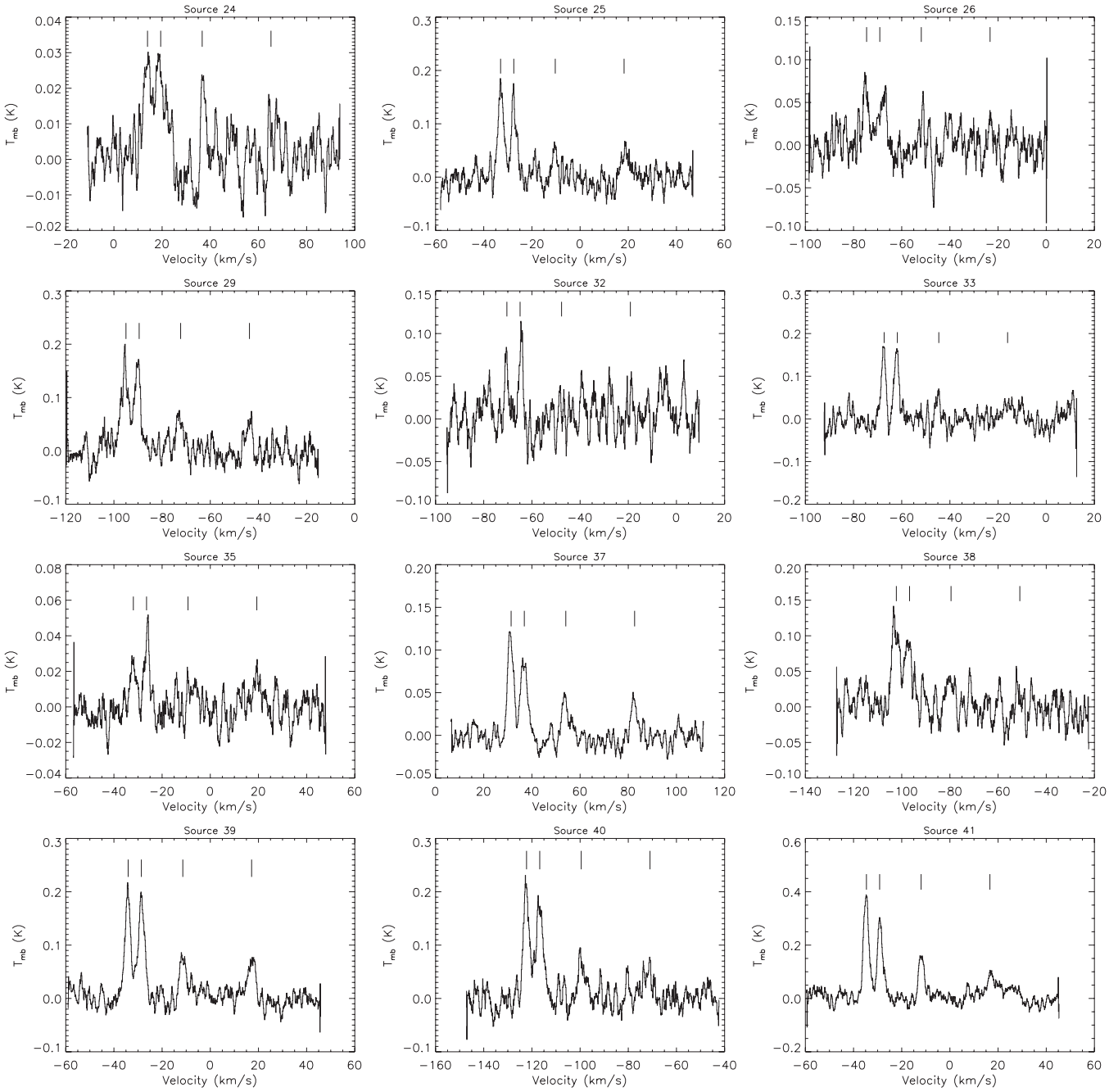

Figure 1. CH_3C_2H(12–11) line spectra for sources with a positive detection; the velocities for the $K = 0$, 1, 2, 3 components are marked with vertical bars. Subsequent panels show the rest of the sources detected; in the case of sources 32, 35, and 38 the $K = 0$, 1 lines were detected, but no valid solution was found for the simultaneous Gaussian fitting of all four components.

statistics for $L/M \gtrsim 1$ may then be the result of a combination of the incipient star formation activity in the clumps that raises the temperature at the levels required to excite the (12–11) transition ($E_U = 37$K) and to desorb a sufficient amount of CH_3C_2H from the the grains ice mantle. Although a more quantitative characterization of the effect would require mapping data in this species, we do not have any; we believe that the qualitative evolutionary interpretation of the changes in CH_3C_2H detection rate with L/M is convincing.

Above the $L/M = 10$ threshold, the energy budget produced internally is such that clumps are all detected in CH_3C_2H.

3.2. The CH_3C_2H Gas Temperature–L/M Relationship

While the CH_3C_2H($J = 12$–11) detection statistics therefore confirms the working hypothesis of L/M as an evolutionary indicator, the information derived from the measured temperature of the CH_3C_2H gas provide a clear quantitative indication in this sense. Figure 2 presents the CH_3C_2H temperature as a function of L/M for the detected sources (all with $L/M > 1$). We find that the derived temperature for all sources detected between $L/M = 1$ and ~10 is $T \lesssim 35$ K irrespective of L/M. For $L/M > 10$, the temperature increases roughly in a linear way with Log(L/M).

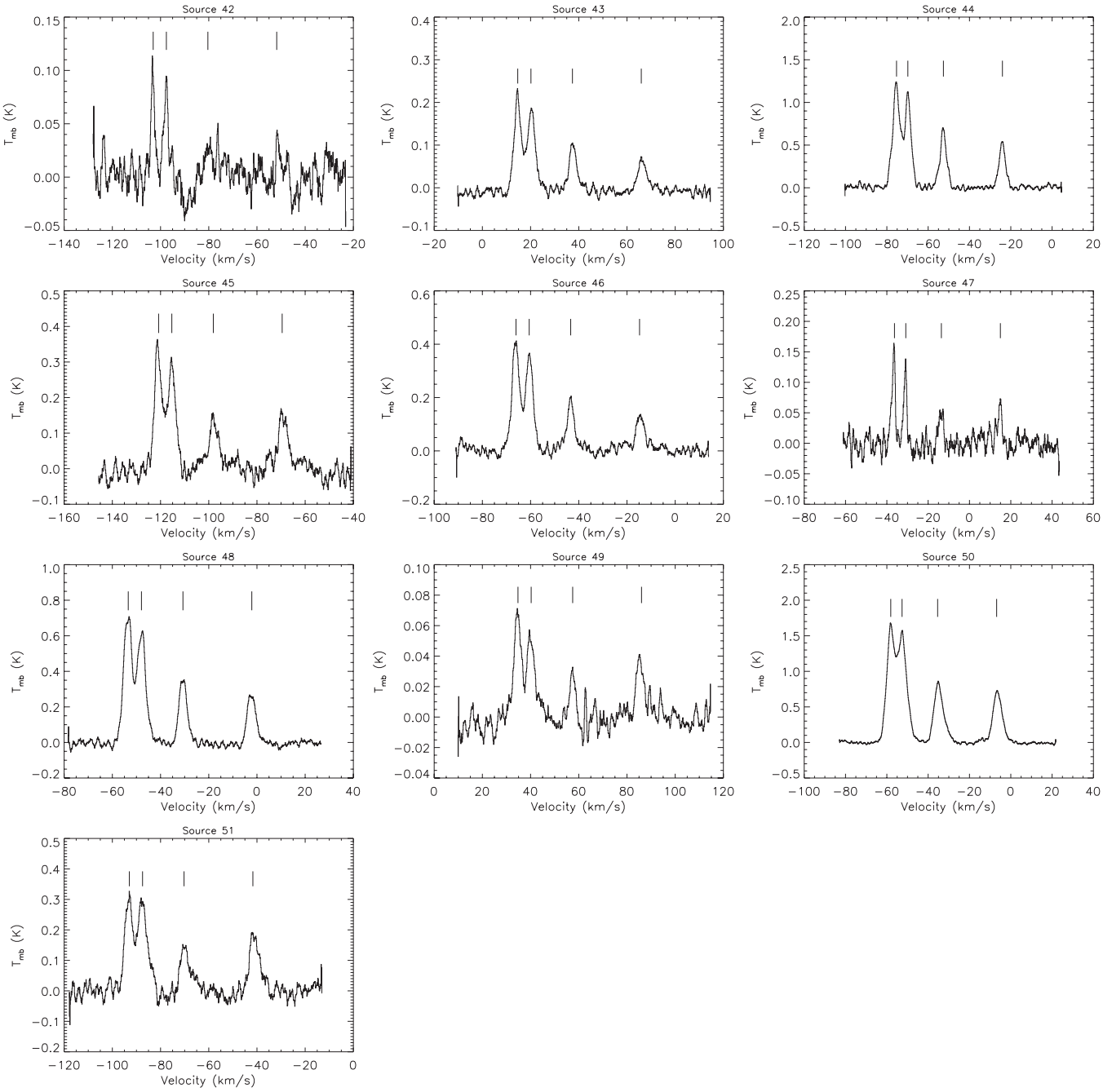

Figure 1. (Continued.)

The *L/M* thresholds that we indicatively put at 1 and 10 to characterize CH_3C_2H detection statistics seem then to have a more robust foundation in change in the energy budget produced by the star formation process in these clumps, also looking at the location of these two *L/M* thresholds in the *L–M* diagram of Figure 3. The cyan line is for $L/M = 1$ and the magenta line is for $L/M = 10$. We already noted how the $L/M = 1$ threshold marks a abrupt change in $CH_3C_2H(J = 12–11)$ detection statistics and corresponds to the upper envelope of the distribution of "pre-stellar" clumps from D. Elia et al. (2016, in preparation); the protostellar sources in this *L/M* range are indistinguishable from the "pre-stellar" sources (other than for the 70 μm counterpart), and indeed $CH_3C_2H(J = 12–11)$ is not detected.

Protostellar clumps leave the *L–M* area occupied by the "pre-stellar" clumps at $L/M = 1$, where new processes must be kicking in to raise the temperature of the inner regions of the clump to levels that allow $CH_3C_2H(J = 12–11)$ detection; however, a further moderate increase in *L/M* up to 10 does not seem to translate into a significant increase of temperature. In a simplified model of a spherical and optically thick dust clump heated by an internal source, we would expect that a raise of a factor 10 (for the same clump mass) of the bolometric luminosity should generate a detectable change in temperature. To quantify this effect, we carried out a set of tests with the dust radiative transfer code TRANSPHERE-1D made publicly available by C.P. Dullemond (adapted from Dullemond et al. 2002) to model the clump SED and temperature structure

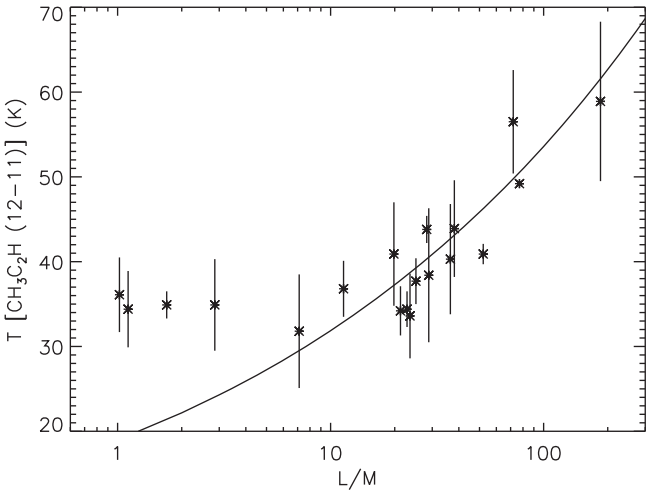

Figure 2. CH_3C_2H rotational temperature as a function of the clump *L/M*. The full line represents the power-law relationship discussed in the text ($T_6 \propto L_{\rm inp}^{0.22}$ discussed in Section 3.2 at constant mass, and is arbitrarily scaled to fit the $L/M \gtrsim 10$ points).

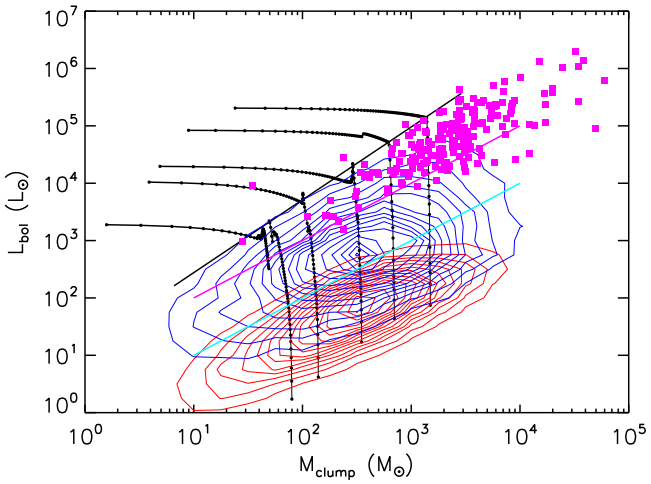

Figure 3. Bolometric luminosity vs. clump mass for Hi-GAL detected clumps from D. Elia et al. (2016, in preparation), where the distribution of "pre-stellar" clumps (no 70 μm counterpart) is indicated with red source density contours and the distribution of protostellar clumps (with 70 μm counterpart) is indicated with the blue contours; tracks are from Molinari et al. (2008). The magenta squares are the subsample of protostellar clumps that have a UCH II counterpart in the CORNISH survey (Purcell et al. 2013) and that have been studied in detail by Cesaroni et al. (2015). The cyan line represents the $L/M = 1$ threshold where CH_3C_2H first detections are found, while the magenta line represent the $L/M = 10$ threshold where $T(CH_3C_2H)$ starts increasing with Log (*L/M*) (see Figure 2).

in spherical geometry. We initially fixed the inner envelope radius to $R_{\rm int} = 200$ au and density gradient $\rho \propto \rho_{\rm int} r^{-1.8}$, varying the internal input luminosities $L_{\rm inp}$ and inner envelope densities. For each run we computed a volume-averaged dust temperature T_6 in the region where $\rho \geqslant 10^6$ cm^{-3}, which is the gas density regime traced by our observations; we note that dust and gas should be thermally coupled in these dense regimes (e.g., Crimier et al. 2010). The two quantities are always related by a power-law of the form $T_6 \propto L_{\rm inp}^{0.22}$; the other model parameters (like inner density or outer radius) affect the proportionality constant and are not interesting here, as we want to characterize a trend in relative terms. The $T_6 - L_{\rm inp}$ relationship is reported in Figure 2 where only the *Y*-axis scaling has been arbitrarily adjusted to fit the points with $L/M \gtrsim 10$; the rise in temperature of such points as a function of *L/M* is remarkably well-reproduced by the model.

The few points with $L/M < 10$ in the figure, however, do not follow this expected trend. We speculate that a possible reason for this is that the assumption of a central heating source in a spherically symmetric clump might not apply for such clumps. In a competitive accretion paradigm where the initial protostellar seed objects do not form at the center of the hosting clumps, our model assumption would not apply; it is quite plausible that a more shallow spatial distribution of heating sources in the clumps may give rise to a warmer (on average) envelope than in the case of a distribution strongly peaked at the clump center. In other words, we are proposing that the constancy of temperature with luminosity in the $1 \lesssim L/M \lesssim 10$ region is not due to a missing increase of temperature as a function of *L/M*, but rather to an excess temperature for relatively low *L/M* due to the formation of protostellar seeds away form the clump center. We will investigate this possibility in detail in a forthcoming paper.

Together with the $CH_3C_2H(J = 12–11)$ detection statistics going virtually to 100%, the rise in gas temperature in Figure 2 for $L/M \gtrsim 10$ suggests a further increase of internal input luminosity at the center of the clump that could be due to an increase in the number of forming YSOs in the clump as well as to their increased luminosity production due to a substantial raise in mass. We believe that the second effect is the dominant one. The magenta large squares in Figure 3 represent the Hi-GAL sources where radio continuum from thermal free–free modeled as H II region emission has been identified by Cesaroni et al. (2015) in the CORNISH survey (Purcell et al. 2013). The remarkable correspondence of the $L/M = 10$ threshold (indicated with the magenta line in Figure 3) with the lower envelope of the distribution of Hi-GAL clumps associated with H II regions, strongly suggests that the rise in gas temperature for $L/M \gtrsim 10$ is mostly due to the appearance of a first ZAMS intermediate/high-mass star in the clump.

Based on the results presented, we propose an evolutionary classification for massive protostellar clumps in which a 70 μm counterpart is detected on the basis of the *L/M* ratio of the clumps:

1. A relatively quiescent phase characterized by $L/M \lesssim 1$, where relatively low-mass objects may be forming. Such seeds of star formation might be either low-mass YSOs or intermediate/massive YSOs in the pristine stages of evolution. These clumps differ from pre-stellar clumps of similar *L/M* in the appearance of a 70 μm counterpart detection; yet the internal input energy does not seem sufficient to warm up the clumps to a detectable level in CH_3C_2H.
2. An intermediate phase where $1 \lesssim L/M \lesssim 10$, in which the clump internal input power due to star formation is sufficient to warm up the envelope and be detectable in CH_3C_2H, but where the increase in input power does not seem to reflect in a temperature increase of the densest portions of the envelope as expected from simple radiative transfer models of spherical clumps heated by a central power source. We argue that this could reflect a phase, consistently with protocluster competitive accretion scenarios in which protostellar seeds are not forming strictly in the center of the clumps but with a more shallow spatial distribution in the clumps; it is plausible

that such a configuration, for which detailed radiative transfer modeling is needed, it is more efficient to warm up the inner regions of the envelope than the centrally peaked input power case. While the luminosity of forming protostars increases, their migration toward denser regions of the clumps makes them less effective in raising the overall envelope temperature.

3. A third phase with $L/M \gtrsim 10$, where the further dramatic increase in luminosity starts warm up the clump more and more. The association of the $L/M = 10$ threshold with the location in the L–M diagram where H II region counterparts to Hi-GAL sources are found (see Figure 3) is an indication that this luminosity increase is related to the birth of the first intermediate/high-mass ZAMS stars in the clusters.

In a parallel effort, we are producing an extensive Montecarlo grid of SED models for synthetic protoclusters embedded in massive clumps spanning masses between 10^2 and 10^5 $M_\odot$; dust temperatures between 10 and 40 K; ages of embedded YSOs cluster from 5×10^4 to 5×10^5 years; and star formation efficiencies up to 40% (S. Molinari & T. Robitaille 2016, in preparation). A preliminary analysis of the properties of the models grid shows that irrespective of the various models parameters, ~80% of the models showing $L/M \geqslant 10$ contain at least one ZAMS star and, for clump masses greater than 10^3 $M_\odot$ (our source selection criterion), the most massive ZAMS star formed is of spectral class B1 or earlier for nearly 100% of the models. A thorough analysis and discussion is deferred to the paper in preparation, but this preliminary analysis seem to confirm that the birth of a B1 ZAMS star (or earlier) is associated with the crossing of the $L/M = 10$ threshold; such stars nominally produce $N_{\rm Ly} \sim 45.11$ (Thompson 1984) that is comparable to the lower values of the Lyman continuum derived by Cesaroni et al. (2015) from the radio flux of the CORNISH counterparts to Hi-GAL clumps.

4. CONCLUSIONS

Observations of the $CH_3C_2H(J = 12–11)$ line toward 51 protostellar massive clumps selected from the Hi-GAL survey provide a clear indication that the ratio between the bolometric luminosity and the mass of a clump can be used to diagnose the star formation evolutionary stage of the clumps. Three stages are identified corresponding to three intervals in L/M values. $L/M \lesssim 1$ in which star formation is either in its very early stages or only low-mass YSOs are forming; $1 \lesssim L/M \lesssim 10$ in which clumps build up their luminosities and temperature, due to ongoing evolution of relatively low-mass protostars; $L/M \gtrsim 10$ in which inner clump gas temperature rises with L/M likely due to the first appearance of intermediate and high-mass ZAMS stars.

This work is based on observations collected at the European Southern Observatory under programmes 096.C-0920(A) and 296.C-5011(A) and is part of the VIALACTEA Project, a Collaborative Project under Framework Programme 7 of the European Union funded under contract #607380, which is hereby acknowledged. The work was also partially supported by the Italian Ministero dell'Istruzione, Università e Ricerca, through the grant "Progetti Premiali 2012—iALMA" (CUP CS2I3000140001).

We thank C. de Breuck and the APEX staff for supporting the APEX observations and V. Rivilla for illuminating discussions on the chemistry of CH_3C_2H.

REFERENCES

Bergin, E. A., Goldsmith, P. F., Snell, R. L., & Ungerechts, H. 1994, ApJ, 431, 674
Billade, B., Nystrom, O., Meledin, D., et al. 2012, ITTST, 2, 208
Bonnell, I. A., Bate, M. R., Clarke, C. J., & Pringle, J. E. 2001, MNRAS, 323, 785
Brand, J., Cesaroni, R., Palla, F., & Molinari, S. 2001, A&A, 370, 230
Cesaroni, R., Pestalozzi, M., Beltrán, M. T., et al. 2015, A&A, 579, 71
Crimier, N., Ceccarelli, C., Alonso-Albi, T., et al. 2010, A&A, 516, 102
de Wit, W. J., Testi, L., Palla, F., Vanzi, L., & Zinnecker, H. 2004, A&A, 425, 937
Dullemond, C. P., van Zadelhoff, G. J., & Natta, A. 2002, A&A, 389, 464
Faustini, F., Molinari, S., Testi, L., & Brand, J. 2009, A&A, 503, 801
Fontani, F., Cesaroni, R., Caselli, P., & Olmi, L. 2002, A&A, 389, 603
Fontani, F., Cesaroni, R., Testi, L., et al. 2004, A&A, 424, 179
Giannetti, A., Brand, J., Sanchez-Monge, A., et al. 2013, A&A, 556, 16
Goldsmith, P. F., & Langer, W. D. 1999, ApJ, 517, 209
McKee, C. F., & Tan, J. C. 2003, ApJ, 585, 850
Miettinen, O., Harju, J., Haikala, L. K., & Pomrén, C. 2006, A&A, 460, 721
Molinari, S., Pezzuto, S., Cesaroni, R., et al. 2008, A&A, 481, 345
Molinari, S., Schisano, E., Elia, D., et al. 2016, A&A, in press (arXiv:1604.05911)
Molinari, S., Swinyard, B., Bally, J., et al. 2010, A&A, 518, L100
Purcell, C. R., Hoare, M. G., Cotton, W. D., et al. 2013, ApJS, 205, 1
Russeil, D., Pestalozzi, M. A., Mottram, J. C., et al. 2011, A&A, 526, 151
Sanchez-Monge, A., Beltrán, M. T., Cesaroni, R., et al. 2013, A&A, 550, 21
Testi, L., Palla, F., & Natta, A. 1999, A&A, 342, 515
Thompson, M. A., & Macdonald, G. H. 2003, A&A, 407, 237
Thompson, R. I. 1984, ApJ, 283, 165
Veneziani, M., Elia, D., Noriega-Crespo, A., et al. 2013, A&A, 549, 130
Veneziani, M., Schisano, E., Noriega-Crespo, A., et al. 2016, A&A, submitted